1.E.3

Nuclear Physics **A248** (1975) 291–316; © *North-Holland Publishing Co., Amsterdam*

RECOIL-DISTANCE MEASUREMENTS OF g-FACTORS FOR ^{24}Mg(2_1^+) AND ^{20}Ne(2_1^+)

R. E. HORSTMAN, J. L. EBERHARDT, H. A. DOUBT, C. M. E. OTTEN and G. VAN MIDDELKOOP

Fysisch Laboratorium, Rijksuniversiteit, Utrecht, The Netherlands

Received 5 May 1975

Abstract: Time-differential recoil-into-vacuum measurements have been performed with a plunger on the first-excited $I^\pi = 2^+$ states of ^{24}Mg and ^{20}Ne. The states were populated by the reactions ^{12}C(^{16}O, α)^{24}Mg and ^{12}C(^{12}C, α)^{20}Ne. The measured anisotropy of the α-γ angular correlation was greatly increased by means of a vertical slit on the annular particle detector. Values of $|g| = 0.51 \pm 0.02$ and 0.54 ± 0.04 have been deduced for the ^{24}Mg and ^{20}Ne g-factors, respectively. The mean lives of these states have been determined as $\tau_m = 2.09 \pm 0.13$ ps and 0.8 ± 0.2 ps, respectively. Various theoretical calculations are discussed and compared with the measured g-factors.

The analysis of the measurement also yields values for the populations of electronic states contributing to the hyperfine interaction. For ^{20}Ne the populations of the different electronic configurations are compared with the results of a separate time-integral measurement, in which the correlations were measured for each ionic state separately. Large fractions of two-electron excited states are found to contribute.

E | NUCLEAR REACTIONS ^{12}C(^{16}O, $\alpha\gamma$), E = 41.7 MeV; ^{12}C(^{12}C, $\alpha\gamma$), E = 36.7 MeV; measured $\alpha\gamma(\theta, t)$ on recoil into vacuum. ^{24}Mg, ^{20}Ne levels deduced g, τ_m, ionic electron configurations. Natural targets.

1. Introduction

It has been amply demonstrated that the hyperfine interaction exhibited by single-electron ions affords the possibility of measuring excited-state g-factors of low-Z nuclei [1–8]). This hyperfine interaction can be measured time differentially on recoil into vacuum by means of a plunger.

The results of the measurements reported here show that the time-differential method may be extended to excited states with shorter lifetimes (1–2 ps) in nuclei of higher Z than hitherto. It is also shown that it is possible to use recoil velocities, for which the fraction of single-electron ions is as low as 10–20 % and for which the fractions of two- and three-electron ions thus dominate. Due to the possibility of excitation many electron configurations may then be expected to contribute to the hyperfine interaction. In the present case, however, there are only a few configurations with mean lives longer than the nuclear lifetime which contribute. The interaction energies of these configurations are also quite well known.

The present paper reports the measurement of the g-factors of the first-excited 2^+ states of ^{24}Mg and ^{20}Ne. These measurements provide experimental values, with

which the basic theoretical assumptions may be tested and which may also be used in the calibration of other experimental methods, for example, the transient field method [9]). In order to distinguish between various nuclear model calculations of g-factors of doubly even $T = 0$ nuclei it is necessary to perform high-precision measurements, since the computed g-factors are not very different for different configuration spaces and different residual interactions.

For ^{24}Mg the precision has been considerably improved over an earlier measurement in this laboratory [10]). This was achieved by improving the statistics and the time-of-flight resolution (steps of 1–2 μm). Moreover, the reliability of the plunger was better determined by continuously monitoring the flatness and position of the target foil with a laser interferometer. It was now possible to follow the oscillation pattern over three periods, compared with little more than one previously. The improved quality of the data leads to a more accurate g-factor and to an improved sensitivity to the hyperfine interactions of other contributing configurations with more than one electron.

The latter information can be used in the analysis of other more difficult measurements for which either the lifetimes are shorter or for which the percentage of single-electron ions is even lower.

2. The experiments

2.1. PRINCIPLE OF THE MEASUREMENTS

Single-electron ions can be formed by stripping off electrons at a high recoil velocity on passage through a foil. As an example of the single-electron hyperfine interaction, doubly even nuclei produced in the first-excited 2^+ state by heavy-ion reactions with spinless particles [e.g. ^{12}C(^{16}O, α)^{24}Mg] are discussed in the following.

The detection of outgoing particles close to 180° in an annular detector selects nuclei excited with their spins perpendicular to the beam axis ($m = 0$ substate population only) and with their momentum directed along this axis (see figs. 1a and 1b). The γ-ray intensity distribution of these selected nuclei has the quadrupole shape shown in fig. 1c at time $t = 0$. The magnetic interaction between the excited nucleus and the electron couples the spin $\boldsymbol{I}$ of the nucleus and the angular momentum $\boldsymbol{J}$ of the electron to a total angular momentum $\boldsymbol{F}$ (see fig. 1b). The effects of this static interaction may be qualitatively understood by the following simple considerations.

Classically the vectors $\boldsymbol{I}$ and $\boldsymbol{J}$ precess around the space-fixed vector $\boldsymbol{F}$ with angular frequency ω. After half a revolution the nuclear spins are distributed over a sphere, from which two cones along the beam axis are missing (fig. 1b). The shape of the angular distribution of the de-excitation γ-rays at this point, shown in fig. 1c for $\omega t = \pi$, resembles the shape generated by nuclei in an $m = 1$ substate. After a full revolution the spins return to their original positions and the resulting γ-ray distribution again has a quadrupole shape. As a function of time the γ-ray distribution thus shows a breathing mode.

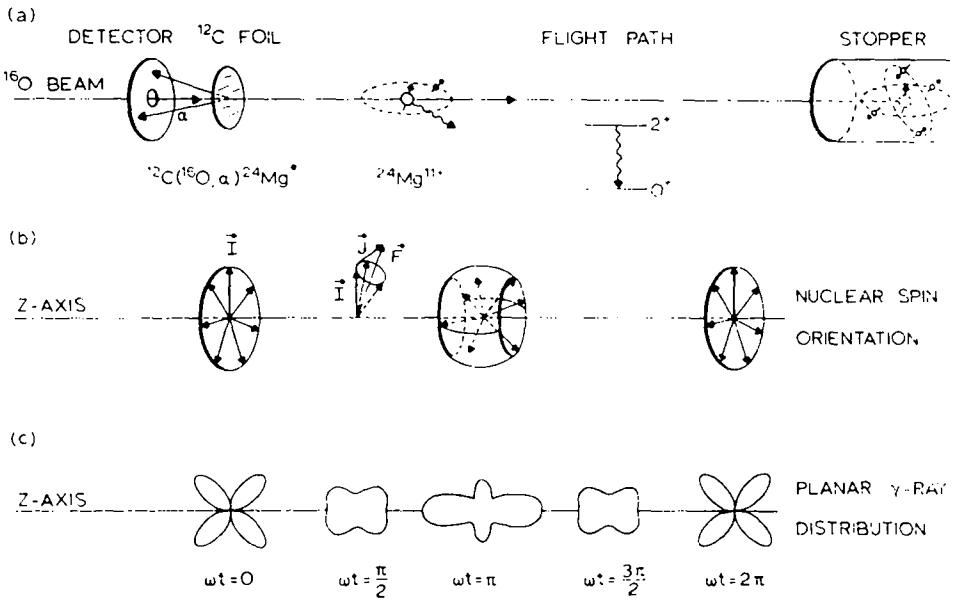

Fig. 1. Simplified classical picture of the nuclear spin deorientation in free ions and its time-differential detection by means of a plunger for the $^{12}C(^{16}O, \alpha)^{24}Mg$ reaction. Part (a) shows the physical arrangement with a single-electron ion of $^{24}Mg(2_1{}^+)$. Part (b) pictures the hyperfine-interaction coupling of the nuclear spin I and the electron spin J to the space-fixed total angular momentum F and shows the resulting nuclear spin orientation after half a precession revolution ($\omega t = \pi$). Part (c) shows the relevant γ-ray angular distribution patterns at different stages in the deorientation.

Quantum mechanically this phenomenon is described as an interference between states with hyperfine energies E_F and $E_{F'}$, where F and F' can take the values $|I-J|$, $|I-J|+1, \ldots, I+J$. This is known as the "quantum beat" [11].

The oscillatory variation in the γ-ray distribution may be sampled by means of a plunger. When the ions reach the stopper the hyperfine interaction is suddenly switched off, due to fast exchange of electrons (10^{-16} s) followed by the filling of electron orbits during slowing down. At this point the nuclear orientation is frozen in and thus the measured γ-ray distribution from nuclei decaying in the stopper is a function of the target-stopper distance. By variation of this distance the nuclear orientation can be measured time differentially.

From the above discussion and fig. 1c it is plausible that the variation in the γ-ray intensity at 0° or 90° to the beam direction may be written

$$I(t) \propto e^{-t/\tau}(1-\cos\omega t), \tag{1}$$

where the finite lifetime τ of the state is taken into account. The experimental determination of such an oscillatory function enables the frequency ω, which is directly related to the nuclear g-factor, to be deduced. A more rigourous treatment is given in subsect. 3.2.

2.2. THE EXPERIMENTAL SET-UP

The first 2^+ states of ^{24}Mg and ^{20}Ne were excited by means of the heavy-ion reactions ^{12}C(^{16}O, α)^{24}Mg and ^{12}C(^{12}C, α)^{20}Ne. Beams of 41.7 MeV $^{16}O^{6+}$ and 36.7 MeV $^{12}C^{5+}$ from the Utrecht 7 MV EN tandem accelerator were focussed through a 2 mm diam. Ta diaphragm onto targets consisting of 500 μg/cm^2 Ni, 300 μg/cm^2 Ag and about 200 μg/cm^2 C. The Ni and Ag layers provided good mechanical strength and heat conduction. The foils were stretched over a 4 mm diam. stainless steel cylinder. Inside this cylinder the position of a precisely fitting stopper rod was adjusted with a simple screw micrometer. The stability and flatness of the foil were monitored by a He-Ne laser† interferometer throughout the experiment. For this purpose the plunger assembly was mounted at an angle of 30° to the beam direction, such that the laser beam could be directed perpendicularly at the beam spot on the target foil (see fig. 2). The distance of closest approach could then be checked whenever desired (subsect. 2.4).

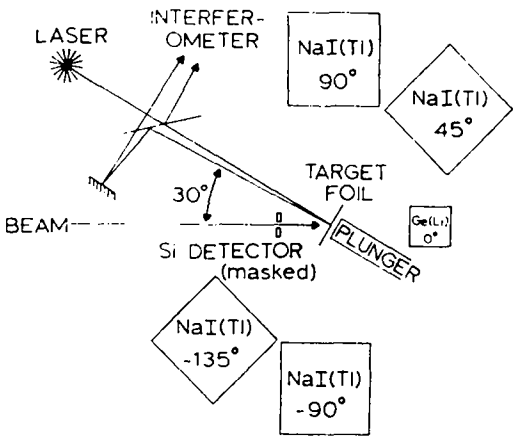

Fig. 2. Schematic horizontal cross section of the experimental set-up showing the α-particle and γ-ray detectors and the orientation of the plunger to the beam.

In the ^{24}Mg measurement γ-rays were detected coincident with α-particles in three 12.7 cm diam. by 12.7 cm long NaI(Tl) crystals at angles of 45°, 90° and −90° with respect to the beam direction and at a distance of 16 cm from the target. For the ^{20}Ne measurement a fourth detector was added at −135° to improve the statistics. A 125 cm^3 Ge(Li) detector was mounted at 0° and at a distance of 11 cm to check the lifetimes of the states.

Outgoing α-particles were detected in an annular 0.2 mm Si surface-barrier detector, which was masked with a vertical slit to improve the experimental γ-ray anisotropy (see subsect. 3.3). The slit subtended angles between 166.3° and 174.4° in the vertical

† Manufactured by Spectra Physics, Calif., USA; λ = 0.6328 μm; 0.5 mW.

plane on either side of the beam and had an opening angle of 9.8° in the horizontal plane.

In the ^{24}Mg experiment a 19 μm mylar foil was mounted in front of the detector to stop inelastically backscattered ^{16}O particles. For ^{20}Ne the foil was removed, in order to keep the α_1 peak at a higher energy than the ^{12}C(^{12}C, p) proton edge.

2.3. TARGET PREPARATION AND MOUNTING

The Ni-Ag supporting foils were prepared by vacuum evaporation of Ag followed by electroplating of Ni. A drop of aquadag † diluted with alcohol was placed on the foil. After drying at about 40 °C the thickness of the ^{12}C layer was determined by weighing. Inspection of the target showed that it was reasonably homogeneous and that thickness variations were less than 1 μm. The target was subsequently mounted on the plunger in dust-free surroundings with the carbon facing the stopper. The measurement was interrupted several times to check that the target remained in good contact with the backing.

The zero distance d_0 of the plunger was measured separately by observation of light shining between the stopper and a precision ruler laid across the cylinder over which the foils were stretched. The zero distance could be measured with a reproducibility of 1 μm and the values obtained were later shown to be consistent with d_0 obtained from fits to the data. The parallelism of the stopper and the foil were estimated to be within 1 μm over the whole stopper. It is an advantage of this plunger that no further adjustment is needed.

To obtain the unperturbed angular correlations for Mg and Ne (i.e. the zero-distance points) a 10 mg/cm^2 layer of Ag was vacuum evaporated onto the carbon side of the target used in the ^{24}Mg measurement. The zero-distance points were then measured with the foil remounted in the plunger.

2.4. EXPERIMENTAL CONDITIONS

The beam current was maintained at 100 ± 20 nA to avoid excessive heating of the target. This current was chosen as a safe limit by observing the target with the laser interferometer and by requiring that the shift in foil position for beam-on and beam-off remained less than 0.3 μm ($\frac{1}{2}$ fringe). This shift was regularly checked and the foil more tightly stretched when necessary, typically once or twice during the experiment. The interferometer was also used to detect the distance of closest approach of the stopper to the foil. This distance was found to be 6–8 μm for the three targets discussed here. Contact was probably caused by dust particles pushing against the foil and was found on slowly decreasing the target-stopper separation to the point where the interference pattern changed.

During the measurements a new distance was selected approximately every 40 min. Most points were measured two or three times. For ^{24}Mg one target was used and

† Manufactured by Acheson Colloiden BV, Scheemda, The Netherlands.

the measuring time was 80 h. In the ^{20}Ne measurement the first target foil deteriorated after 70 h. Both target and stopper were replaced for a second run of 70 h.

After one of the experiments a run was performed with the stopper only and the carbon deposit on the stopper was found to be less than 5 μg/cm^2. In spite of good vacuum (an ion-pump mounted directly below the target showed 2×10^{-6} Torr) a thin layer of 13 μg/cm^2 was deposited on the beam side of the plunger foils (see fig. 4).

2.5. DATA COLLECTION

The data collection system is similar to the system briefly described in ref. [12]. Fast timing signals from the α-particle detector and the γ-ray detectors were used to start and stop the time-to-amplitude converters (TAC). These signals were generated by timing filter amplifiers (TFA) followed by constant fraction timers (CFT), as shown in fig. 3. The output signals of the TAC units were mixed and fed into the "time" analogue-to-digital converter (ADC). Each TAC output was also followed by a single-channel analyzer (SCA), the window of which selected the time range accepted.

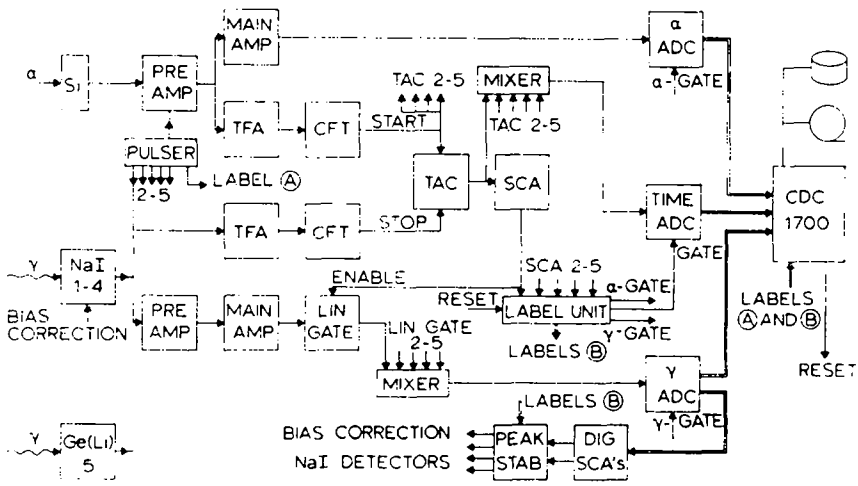

Fig. 3. Scheme of the data collection system. Only one γ-ray detection channel is given in full. The channels for the NaI(Tl) detectors 2–4 and the Ge(Li) detector channel (5) are identical to that of NaI(Tl) detector 1.

The output pulses of the SCA units also served to generate a binary label-bit pattern in the label unit to distinguish different γ-ray detectors and to open linear gates in the analogue channels. The linear gate outputs were mixed and fed into the γ-ADC. The purpose of these gates was to prevent pulse pile-up and cross-talk. The signals from the α-particle detector after amplification were directly fed into the α-ADC. The label unit also provided gate pulses for the three ADC units. The digitized α-particle, γ-ray and time signals were fed into a CDC 1700 computer together with label-bit patterns

defining pairs of coincident detectors. To avoid changes in the labels during conversion the label unit rejected all further pulses until it was reset by the computer.

The experiment was monitored with an on-line sorting procedure, using a disk for spectrum storage, while the raw data were written event by event on magnetic tape for later off-line analysis.

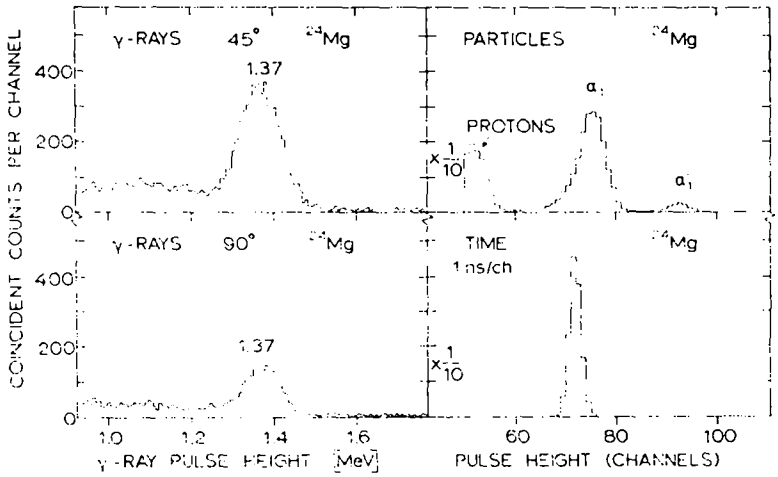

Fig. 4. Coincident γ-ray, α-particle and time spectra for ^{24}Mg summed over several runs. For the γ-ray spectra measured at 45° and 90° to be beam direction randoms have been subtracted. Note the α_1' peak due to carbon build-up on the beam side of the target.

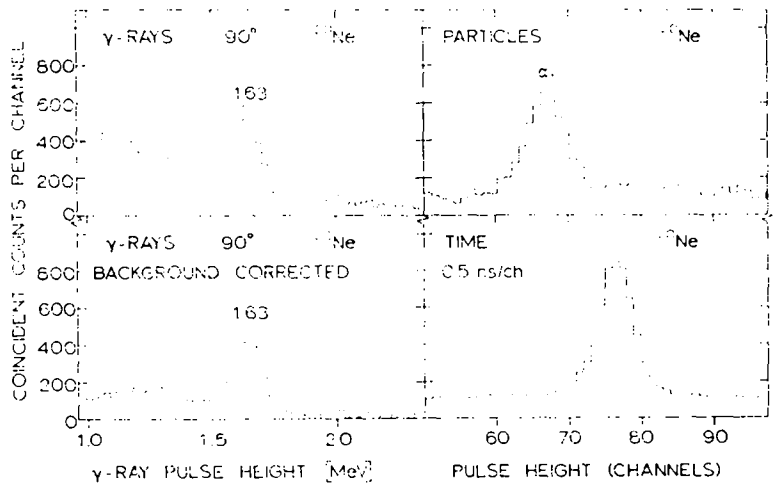

Fig. 5. Coincident γ-ray, α-particle and time spectra for ^{20}Ne summed over several runs. The upper random-corrected γ-ray spectrum at 90° to the beam direction is not corrected for coincident background from reactions in the Ni-Ag supporting foil (see the corresponding background in the particle spectrum). The lower γ-ray spectrum is corrected for this coincident background.

Four peak-stabilizers were steered by two labelled digital SCA units set symmetrically about the γ-ray peak in the NaI(Tl) spectra. Gain variations in the photomultipliers were automatically adjusted by small bias corrections and were kept below 2%.

As a check on the electronics a pulser unit sent coincident pairs of pulses to the α-particle preamplifier and to each of the γ-ray preamplifiers in turn. These test signals were labelled separately to distinguish them from the γ-ray and α-particle spectra. In this way both the proper functioning of the labelling system and the absence of cross-talk and pile-up could be monitored. Typical α-particle, γ-ray and time spectra for ^{24}Mg and ^{20}Ne are shown in figs. 4 and 5. The time resolution obtained was 4 ns (FWHM).

3. Results and interpretation

3.1. DATA ANALYSIS

In the slit geometry it is necessary to measure the γ-ray intensity at 90° for maximum anisotropy (see subsect. 3.3). For reasons of normalization and amplification of the effect the γ-ray intensity at 45° was also measured. Since the stopped and flight fractions are indistinguishable at 90° large NaI(Tl) detectors were used. The ratio $R(t)$ of coincident γ-ray counts measured at 90° and −90° to those at 45° and −135°,

$$R(t) \equiv \frac{W(90°, t) + W(-90°, t)}{W(45°, t) + W(-135°, t)}, \tag{2}$$

behaves as a function of time (target-stopper distance) as a damped oscillation, approximately according to eq. (1) but with the inclusion of the flight fraction, for which the oscillation effects are almost washed out. These ratios R obtained for ^{24}Mg and ^{20}Ne are plotted as a function of target-stopper distance in figs. 6 and 7. To obtain the ratios R the following corrections have been applied to the contents of the photopeaks.

The angle-dependent γ-ray absorption in the plunger chamber was determined by replacing the target foil by ^{60}Co and ^{88}Y radioactive sources.

All spectra were corrected for random coincidences. This yielded clean spectra for ^{24}Mg (see fig. 4). For the ^{20}Ne measurement, however, there remained an appreciable coincident background due to reactions in the Ni backing. This problem did not arise in the ^{24}Mg experiment because the α-particle detector was shielded against backscattered projectiles with a mylar foil (see subsect. 2.2).

To measure this background, a separate run on a bare Ni-Ag foil was performed. The coincident particle spectrum showed a smoothly decreasing slope. Gamma-ray spectra coincident with two windows set at the ^{20}Ne α_1 peak position and at slightly higher energy showed close similarity but differed in intensity by a factor of 1.5. The ^{20}Ne γ-ray spectra were corrected for the coincident background by subtracting 1.5 times the spectrum generated with the off-α-peak window. The effect of this correction is shown in fig. 5.

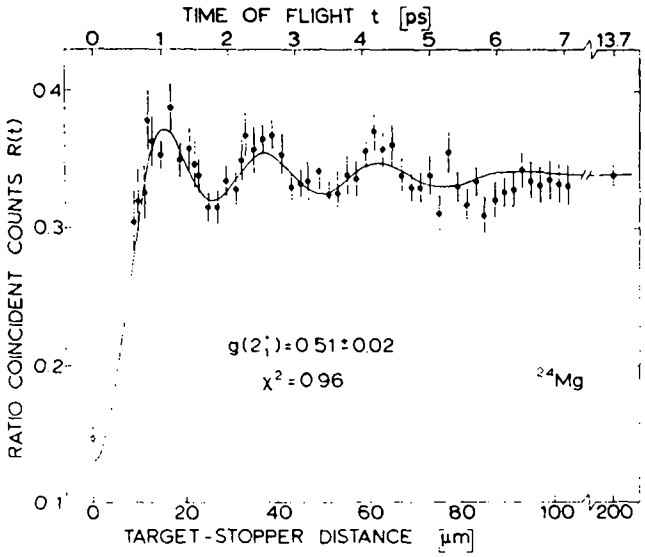

Fig. 6. Ratio of coincident counts $R(t)$ as a function of perpendicular target-stopper distance for ^{24}Mg. The curve is a least-squares fit to the data (fit II, see subsect. 3.4.1). The zero-distance point was not used in the fit.

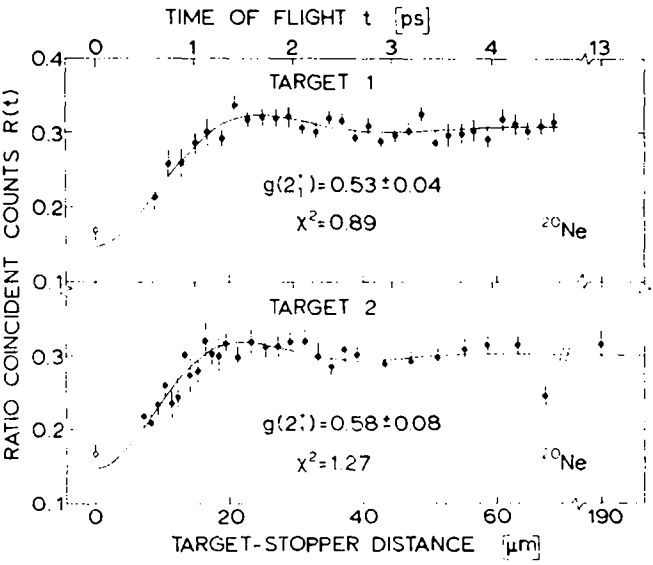

Fig. 7. Ratio of coincident counts $R(t)$ as a function of perpendicular target-stopper distance for ^{20}Ne for both targets separately. The curves are least-squares fits to the data (fit I, see subsect. 3.4.1). The zero-distance point was not used in the fits.

No relativistic corrections were necessary because the effect is mainly determined at 90° where these corrections are of second order.

3.2. ELECTRON CONFIGURATIONS AND FIELDS

All possible configurations with lifetimes longer than or comparable to the nuclear lifetime and with up to three electrons in the 1s, 2s and 2p orbits are displayed in table 1. The four-electron configurations have very weak hyperfine interactions or none. Electron configurations with orbits higher than 2s or 2p occupied need not be considered because of Bohr's matching principle [13]), i.e. electrons with orbital velocities lower than the translational velocity of the moving ion will be stripped off. For ^{24}Mg and ^{20}Ne ions emerging from the targets at recoil velocities of $v/c = 0.06$ charge states with more than four electrons are only weakly populated (less than 2 %).

TABLE 1

Possible long-lived atomic states for $n = 1$ and $n = 2$ in isolated ions

Configuration	Term	HFI [a])	τ_m(Mg)	τ_m(Ne)
Single-electron ion				
$(1s)^1$	$^2S_{\frac{1}{2}}$	s	∞	∞
$(2s)^1$	$^2S_{\frac{1}{2}}$	w	40 ns [b])	120 ns [b])
$(2p)^1$	$^2P_{\frac{1}{2},\frac{3}{2}}$	w	77 fs [c])	160 fs [c])
Two-electron ion				
$(1s)^2$	$^1S_0$	n	∞	∞
$(1s)^1(2s)^1$	$^3S_1$	s	30 ns [b])	110 ns [b])
	$^1S_0$	n	20 μs [b])	130 μs [b])
$(1s)^1(2p)^1$	$^3P_0$	n		
	$^3P_1$	s	20 ps [d])	140 ps [d])
	$^3P_2$	s	4 ns [b])	5 ns [b])
Three-electron ion				
$(1s)^2(2s)^1$	$^2S_{\frac{1}{2}}$	w	∞	∞
$(1s)^2(2p)^1$	$^2P_{\frac{1}{2},\frac{3}{2}}$	w	1.3 ns [e])	1.8 ns [e])
$(1s)^1(2s)^1(2p)^1$	$^4P_{\frac{1}{2},\frac{3}{2},\frac{5}{2}}$	s	10 ns [e])	10 ns [e])
$(1s)^1(2p)^2$		s		

[a]) Hyperfine interaction (HFI), strong (s), weak (w), null (n).
[b]) Ref. [39]). [c]) Ref. [40]). [d]) Ref. [41]). [e]) Refs. [23, 24]).

In the Russel-Saunders LS coupling scheme the electron spins and the orbital angular momenta couple to $\boldsymbol{S}$ and $\boldsymbol{L}$, respectively, and the total angular momentum is given by $\boldsymbol{J} = \boldsymbol{L} + \boldsymbol{S}$. In atomic physics notation such a state is denoted by $^{2S+1}L_j$.

Other possible terms not listed in table 1 are Auger unstable or decay by fast X-ray transitions, for which the following selection rules apply: $\Delta S = 0$ and $\Delta L = 0, \pm 1$,

with $\Delta l = \pm 1$ for the electron causing the transition, and thus $\Delta J = 0, \pm 1$ but with the exception of $J = 0 \rightarrow J = 0$. Excited electron configurations which decay by allowed transitions or, for high excitation energies, by Auger processes have lifetimes of the order of 10^{-15} s, i.e. short compared to the nuclear lifetime. Excited states without the possibility for allowed decay generally have lifetimes long compared to the nuclear lifetime (see table 1) and may contribute to the hyperfine interaction. The main contributions come from configurations with unpaired 1s electrons, which produce high magnetic fields at the nucleus. The states that need to be taken into account in the analysis of the present experiments are listed in table 2, which also includes the total number of components and the highest frequency component for each term relative to that (ω_{1s}) of a single 1s electron.

TABLE 2

Hyperfine interaction coefficients a_J used in the analysis of the experiments

Configuration	Term	No. of frequencies	ω_{max}/ω_{1s}	a_J (rad · ps^{-1})	
				Mg	Ne
Single-electron ion [a])					
$(1s)^1$	$^2S_{\frac{1}{2}}$	1	1.00	2.76	1.60
$(2s)^1$	$^2S_{\frac{1}{2}}$	1	0.125	0.35	0.20
Two-electron ion					
$(1s)^1(2s)^1$	$^3S_1$	3	1.11	1.53 [b])	0.89 [b])
$(1s)^1(2p)^1$	$^3P_2$	5	1.02	0.71 [a])	0.41 [a])
	$^3P_1$	3	0.52	0.72 [a,c])	0.42 [a,c])
Three-electron ion [d])					
$(1s)^2(2s)^1$	$^2S_{\frac{1}{2}}$	1	0.10	0.28	0.15

[a]) Ref. [15]).
[b]) Relativistic Hartree-Fock calculation quoted in ref. [21]).
[c]) Average value of *jj* and *LS* coupling.
[d]) Screening calculated in the alkali approximation with the effective quantum numbers taken from ref. [43]).

The effect of the hyperfine interaction of an electronic state on the angular correlation as a function of time is given by the attenuation coefficients [eq. (298); ref. [14])]

$$G_k(t) = \sum_{FF'} C_{FF'} \exp\left\{-\frac{i}{\hbar}(E_F - E_{F'})t\right\}, \tag{3}$$

where

$$C_{FF'} = (2F+1)(2F'+1)\begin{Bmatrix} F & F' & k \\ I & I & J \end{Bmatrix}^2 \Big/ (2J+1),$$

$$\frac{i}{\hbar}(E_F - E_{F'}) = \omega_{FF'} = \{F(F+1) - F'(F'+1)\}\frac{a_J}{2\hbar}g. \tag{4}$$

The quantities $\omega_{FF'}$, g and a_J represent, respectively, the Larmor frequency, the

nuclear g-factor and the interaction energy defined by Kopfermann [15]) for $g = 1$. Eq. (3) is calculated under the assumption of a randomly oriented (i.e. isotropic) hyperfine interaction.

The attenuation coefficients for the sum of the fractions of nuclei decaying in flight and in the stopper are given by

$$G_k(t) = \sum_i \alpha_i \sum_{FF'} C_{FF'} \left\{ e^{-t/\tau} \cos \omega^i_{FF'} t + \frac{1 - e^{t/\tau}(\cos \omega^i_{FF'} t - \omega^i_{FF'} \tau \sin \omega^i_{FF'} t)}{1 + (\omega^i_{FF'} \tau)^2} \right\}, \qquad (5)$$

where α_i is the population of the ith electronic state. To illustrate the effect of this function, fig. 8 shows the ratio $R(t)$ calculated as a function of target-stopper distance for each electronic state given in table 2 separately with a population $\alpha = 30\,\%$. The curve shown for the $(1s)^1$; $^2S_{\frac{1}{2}}$ state, for example, is the measured effect that would be expected in the present ^{24}Mg experiment, if 30 % of the ions were in the single-electron ground state and the rest were distributed between the zero-electron and the ground-state two-electron charge states. The actual fit from fig. 6 is also included for comparison.

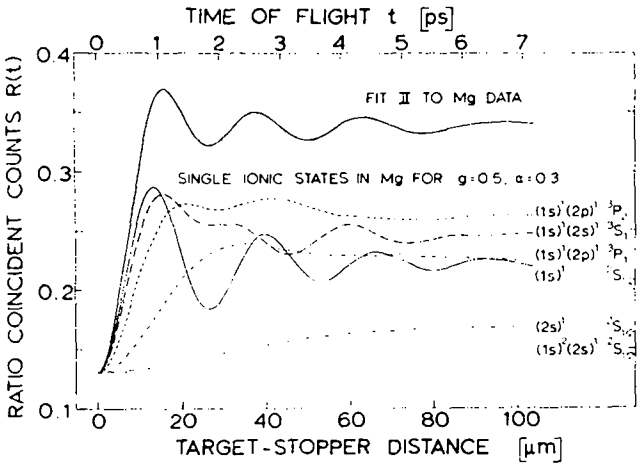

Fig. 8. Ratio of coincident counts $R(t)$ plotted as a function of the time of flight t both for fit II to the Mg data (above) and for each ionic state of table 2 separately with a g-factor $g = 0.5$ and a population of the state of $\alpha = 0.3$ (below). The scale below the figure is the perpendicular target-stopper distance.

3.3. THE VERTICAL SLIT

In reactions with spinless particles in a collinear geometry, i.e. when the outgoing particles are detected at 180° to the beam direction (z-axis), the final excited nucleus has only $m = 0$ magnetic substates populated. Hence the angular correlation of a subsequent $2^+ \to 0^+$ γ-ray transition shows large anisotropy. Since the particle detector has a finite size, however, $m = \pm 1$ substates may also be populated, especially

when the incoming particles have high angular momenta [l = 6–12; ref. [16])]. In this case an angular correlation with a lower anisotropy will result.

This effect can be clearly demonstrated by the measurement of the direction of the symmetry axis of the correlation for the $^{12}C(^{12}C, \alpha\gamma)^{20}Ne$ reaction as a function of the angle of α-detection. For this purpose a position-sensitive detector subtending angles between 117° and 161° with respect to the beam axis was used. The position along the detector was converted to the angle with respect to the beam direction by measuring the position of the α-radiation shadow cast by a rotatable needle on the position-sensitive detector by an ^{241}Am-^{244}Cm source centred in the target chamber. The result of the measurement is displayed in fig. 9. From the fast rotation of the angular correlation symmetry axis with α-particle detection angle it is obvious that the correlation measured with a relatively large-angle annular detector shows reduced anisotropy.

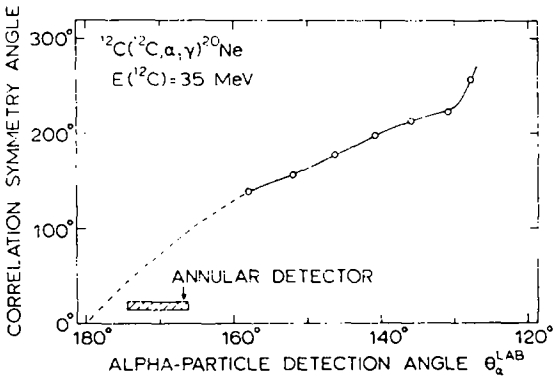

Fig. 9. The γ-ray angular correlation symmetry axis plotted versus the α-particle detection angle for the $^{12}C(^{12}C, \alpha\gamma)^{20}Ne$ reaction. The symmetry axis rotates a factor 7.5 faster and in the opposite direction to the ^{20}Ne recoil direction. For the position of an annular particle detector shown the corresponding γ-ray angular correlation would be attenuated.

For a theoretical description of the γ-ray angular correlation for particles not detected at 180°, it is convenient to choose a new coordinate system, in which the x-axis is taken along the beam direction and the z-axis is taken perpendicular to the reaction plane in the direction $\boldsymbol{k}_i \times \boldsymbol{k}_o$, where $\boldsymbol{k}_i$ and $\boldsymbol{k}_o$ represent the directions of the incoming heavy and outgoing light particles, respectively. The angular correlation can be written as a function of the azimuthal and polar angles ϕ and θ,

$$W(\theta, \phi) = \sum_{kN} B_k^N(1) G_k(t) A_k(2) Y_k^N(\theta, \phi), \tag{6}$$

with summation over $k = 0, 2, 4, \ldots$ and $N = -k, -k+2, \ldots +k$. The $A_k(2)$ represent the angular correlation coefficients for the transition in the final nucleus and $Y_k^N(\theta, \phi)$ are spherical harmonics. The coefficients $B_k^N(1)$ are given by

$$B_k^N(1) = \sum_{mm'} (-1)^m \langle m|\rho^I|m'\rangle \begin{pmatrix} I & I & k \\ m' & -m & N \end{pmatrix} \Big/ \sum_{mm'} (-1)^m \langle m|\rho^I|m'\rangle \begin{pmatrix} I & I & 0 \\ m' & -m & 0 \end{pmatrix}, \tag{7}$$

where the $\langle m|\rho^I|m'\rangle$ are the elements of the density matrix of the substates m after formation of the excited state I [cf. eq. (33); ref. [14])]. These elements depend on the reaction mechanism and thus must be determined experimentally. In the chosen coordinate system, however, for natural parity states excited in reactions with spinless particles, the Bohr theorem [17]) states that only $I-m$ = even substates are populated. Eq. (6) may be derived† from eq. (207) in ref. [14]). For a $2^+ \to 0^+$ transition in the final nucleus $W(\theta, \phi)$ becomes proportional [18]) to $\sin^2\theta$.

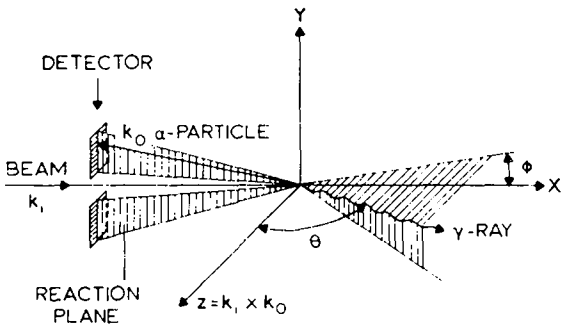

Fig. 10. The slit geometry characterized by a vertical reaction plane defined by the beam direction ($\boldsymbol{k}_1$) and the detected outgoing α-particle ($\boldsymbol{k}_0$). The horizontal z-axis is perpendicular to the beam direction. The azimuthal angle ϕ in the (x, y) plane and the polar angle θ with respect to the z-axis are also indicated.

This proportionality means that for point detectors the correlation function drops to zero along the z-axis. If the particles are detected not in a point but along a vertical line through the beam axis (see fig. 10), the reaction plane is fixed vertically and the z-axis is fixed in the horizontal plane at 90° to the beam direction ($\theta = 0°$). Thus in the case of a vertical mask on the annular detector a maximum anisotropy for the unperturbed correlation will be obtained. The density matrix elements, however, also depend on the detection angle of the α-particles. On averaging over the detection

† The density matrix in eq. (7), which has a simple form for the present coordinate system and reaction [four unknown parameters [18])], is transformed to a system with arbitrary z' axis (for example in the direction of an external magnetic field) as

$$\langle \mu|\rho^I|\mu'\rangle = \sum_{mm'} \langle m|\rho^I|m'\rangle D^J_{m'\mu'}(z \to z') D^{J*}_{m\mu}(z \to z')$$
$$= \sum_{k\tau N} B^N_k \begin{pmatrix} I & I & k \\ \mu' & -\mu & \tau \end{pmatrix} D^k_{-N-\tau}(z \to z')$$

where $D^J_{m'\mu'}(z \to z')$ is an element of the matrix that carries out a rotation of the quantization system z into a system z' [eq. (9); ref. [14])]. This density matrix replaces the density matrix $\langle m'|\rho(k_1)|m'\rangle$ in eq. (207) of ref. [14]). Eq. (6) can now be derived with eqs. (208), (209) and (298) in ref. [14]).

angle and using the Bohr theorem eq. (6) can be rewritten as

$$W(\theta, \phi) = Y_0^0 + A_2 Q_2 G_2(t)[\overline{B_2^0}\, Y_2^0(\theta, \phi) + 2\overline{B_2^2}\, \mathrm{Re}\,\{Y_2^2(\theta, \phi)\}]$$
$$+ A_4 Q_4 G_4(t) \left[\left(\frac{1}{12}\sqrt{14} - \tfrac{5}{12}\overline{B_2^0}\right) Y_4^0(\theta, \phi) + \frac{1}{3}\sqrt{15}\,\overline{B_2^2}\, \mathrm{Re}\,\{Y_4^2(\theta, \phi)\}\right.$$
$$\left. + 2\overline{B_4^4}\, \mathrm{Re}\,\{Y_4^4(\theta, \phi)\}\right], \tag{8}$$

where the geometrical attenuation coefficients Q_k have been introduced [see ref. [14]), p. 1691]. Note that the averaged coefficients $\overline{B_4^0}$ and $\overline{B_4^2}$ do not appear in eq. (8), since they are related to the coefficients $\overline{B_2^0}$ and $\overline{B_2^2}$. For symmetry reasons the coefficients $\overline{B_0^2}$, $\overline{B_2^2}$ and $\overline{B_4^2}$ are real and may be determined experimentally. This was carried out with the zero-distance-point target (see subsect. 2.3) in separate unperturbed angular correlation measurements, in which the slit was taken successively at 0°, 45° and 90° to the γ-ray detector plane. In this way the correlations were measured three-dimensionally. The result of the measurement for ^{20}Ne is displayed in fig. 11.

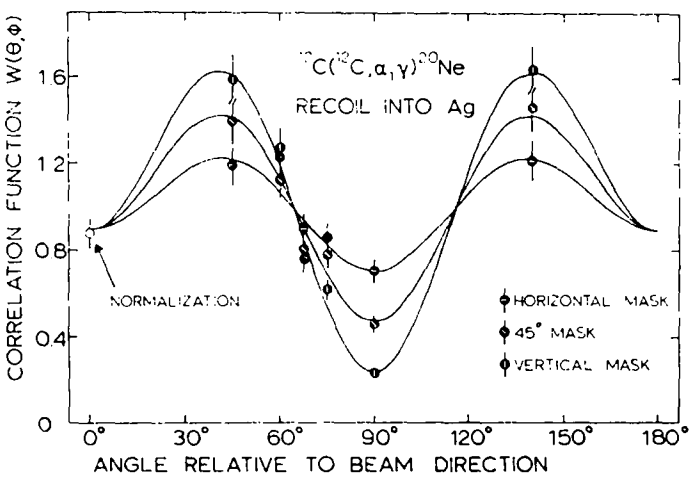

Fig. 11. Alpha-gamma angular correlations with the ^{20}Ne reaction measured for the three orientations of the rectangular mask. The three curves were fitted simultaneously to the experimental points normalized to the coincident yield at 0°.

The figure clearly shows that the minimum anisotropy is found, as expected, for the horizontal slit, for which the z-axis is perpendicular to the horizontal γ-ray plane. The correlation measured for the 45° slit corresponds roughly to the correlation measured for the unmasked detector. The $\overline{B_k^N}$ parameters, extracted by a simultaneous fit to the three correlations with allowance for the finite width of the slit, were used in the subsequent analysis of the plunger data.

3.4. RESULTS

3.4.1. The g-factors. The corrected data from the ^{24}Mg and both ^{20}Ne measurements (see subsect. 3.1) are shown in figs. 6 and 7. The perpendicular target-stopper distances are given below the figures, whereas above the figures the actual time of flight of the ions from the target to the stopper along the beam axis is given.

A computer program was written to perform a non-linear least-squares fit of the function $R(t)$ for the electronic states of table 2 to the data points, taking into account the finite width of the slit. An uncertainty of 1 μm in the setting of the micrometer was also assumed.

Three types of fit (I–III) were performed for ^{24}Mg. In the first the populations of the $^3S_1$, $^3P_2$ and $^3P_1$ states, which have about the same excitation energy, were assumed to be statistically distributed with weights $2J+1$. The other free parameters in the fit were the population of the single-electron ground state, the g-factor and the zero distance of the plunger i.e. four free parameters in total and 53 experimental points. In the second type of fit the populations of the $^3S_1$ state and of the two ^3P states taken together were allowed to vary independently. In the third type the populations of all three triplet states were allowed to vary independently. The result of fit II is shown in fig. 6. For ^{20}Ne only the first type of fit, with the smallest number of free parameters, was stable and was used for both targets (in each case 31 experimental points, see fig. 7).

For completeness small, fixed contributions from the single-electron excited state and the three-electron ground state, which have small interaction coefficients (see table 2 and fig. 8), were included in the fits. The effect on the fitted parameters was negligible, but the value of χ^2 became marginally worse. For ^{20}Ne the amounts of these contributions were taken from a separate integral measurement involving charge-state separation in a magnetic spectrograph (see subsect. 3.4.3). For ^{24}Mg the amplitudes of the two contributions were fitted separately to the data. This gave upper limits for the populations $\alpha[(2s)^1]$ and $\alpha[(1s)^2(2s)^1]$ of 0.08 and 0.11, respectively, at the three standard deviation limit. The latter limit is rather lower than the population expected from the three-electron fraction. A value of 0.10 has been used in the analysis (see table 4).

The g-factors extracted from the fits for ^{24}Mg and ^{20}Ne are displayed at the bottom of table 3. This table also details the separate contributions (treated independently) to the final quoted errors of 4 % and 8 %, respectively. The values of the populations α extracted for the various electronic states for the different types of fit are given in table 4 and are discussed in subsect. 3.4.3.

The value of the g-factor for ^{24}Mg did not depend very strongly on the type of fit performed i.e. on the relative populations of the excited two-electron states. Fits II and III gave almost identical results i.e. no new information was obtained from the six-parameter fit. Fit I gave a value that was 2.8 % higher than fit II and the fit was somewhat poorer with a χ^2 value of 1.1 compared to 1.0. The value of the g-factor quoted in table 3 is the average of the values obtained for fits I and II. The spread of

TABLE 3

Error analysis and final results for the g-factors

Source of error	Contribution to error (%)		
	$^{24}Mg(2_1^+)$	$^{20}Ne(2_1^+)$	
		target 1	target 2
Statistics	2.1	6.3	7.9
Zero distance	1.7	3.3	8.8
Target thickness	2.3	2.3	2.3
Lifetime	0.2	2.4	3.9
Two-electron analysis	1.4	1.4 [a])	1.4 [a])
$a_J(^3S_1)$	0.6	0.6 [a])	0.6 [a])
$a_J(^3P_1)$	0.3	0.3 [a])	0.3 [a])
Coincident background	0.0	2.0	6.0
Total error	3.9	8.2	14.1
g-factor g_1^+	0.51 ± 0.02 [b])	0.53 ± 0.04 [c])	0.58 ± 0.08 [c])
		mean 0.54 ± 0.04 [c])	

[a]) From the ^{24}Mg analysis.
[b]) Average of the values obtained for fits I and II.
[c]) Fit I.

1.4 % in the g-factor has been taken to represent the uncertainty in the two-electron analysis (table 3). For ^{20}Ne this is probably an overestimate, since more ions are in the $(1s)^1$ state.

The uncertainties in the $\overline{B_k^N}$ coefficients and the absorption correction introduce negligible errors in the g-factor. The other sources of error are discussed in the following subsection.

The values of the function $R(t)$ for ^{24}Mg and ^{20}Ne at zero distance were completely determined by the measurements of the $\overline{B_k^N}$ coefficients (subsect. 3.3). The zero-distance points measured with the plunger (see subsect. 2.3) are shown in figs. 6 and 7 for illustration but were not included in the fits. The zero-distance point for ^{24}Mg, unlike the rest of the ^{24}Mg data for which the anisotropy was lower, had to be corrected for coincident background at 90°. The zero-distance points show reasonable agreement with the result of the measurement of the full correlation, although for these two points the background correction may be slightly underestimated.

3.4.2. Error analysis (see also table 3).

(*i*) *Zero distance.* Values for the zero distances d_0 were derived from the fits for the three experiments with an uncertainty of about 1 μm. The values measured by eye in the manner discussed in subsect. 2.3 were about 2 μm nearer the stopper. The value derived from the ^{24}Mg lifetime measurement coincided with the result of the measurement by eye. This is good agreement within the errors. A weighted mean of these four values was taken for d_0 for the ^{24}Mg target and the first ^{20}Ne target since

these were measured with the same stopper. A mean of the value from the g-factor fit and the measurement by eye were taken for the second ^{20}Ne target.

Effects caused by the fast decay of higher-lying electronic states within the nuclear lifetime would give an apparent shift of the zero distance towards the stopper [see for example the treatment of Bosch and Spehl [19])]. The present measurements indicate an upper limit of 150 fs for the possible delay in the switching-on of the hyperfine interaction in Mg and Ne ions.

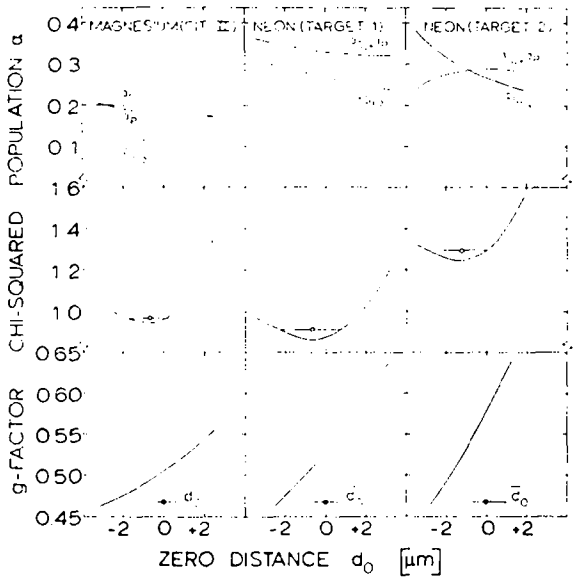

Fig. 12. The dependence of the g-factor, χ^2 and the populations α of the ionic states on the zero distance d_0 of the plunger. The averaged values of d_0 (see subsect. 3.4.2) have been normalized to $d_0 = 0$ and the uncertainties are indicated. The d_0 values with the errors obtained from the fits are indicated in the χ^2 plots.

The dependence of the g-factor on the zero distance d_0 for the three targets is plotted in fig. 12, which also includes the dependence of χ^2 and of $\alpha(1s)$ and $\alpha(^3S+{}^3P)$. These plots demonstrate the confidence with which d_0 may be fitted and also suggest that previous experimenters may have underestimated the importance of this source of error.

(*ii*) *Target thickness.* The recoil velocities of the ^{24}Mg and ^{20}Ne ions were calculated from the kinematics taking into account the thickness of the Ni-Ag supporting foil, the thickness of the ^{12}C target, the angle of the target with respect to the beam and the opening angle of the α-particle detector. The values obtained for v/c were $(5.58\pm0.13)\,\%$ and $(5.69\pm0.13)\,\%$, respectively. The main uncertainty in the velocities stems from the uncertainty in the thickness of the carbon layer. An uncertainty of 50 % was assumed in the thickness of 200 μg/cm^2 measured by weighing, to allow for possibly uneven deposit of carbon during drying (see subsect. 2.3).

(*iii*) *Lifetimes*. The values 2.09 ± 0.13 ps and 1.04 ± 0.07 ps were taken for the lifetimes of the first 2^+ states in ^{24}Mg and ^{20}Ne, respectively. For ^{24}Mg the value is that of the present work (subsect. 3.4.4). The error in the lifetime hardly contributes to the error in the g-factor for ^{24}Mg (table 3). On treating the lifetime of ^{24}Mg as a free parameter in the g-factor fit with d_0 already determined, a consistent value of 2.1 ± 0.4 ps was found.

For the ^{20}Ne measurement, however, for which the oscillation is quickly damped out by the short lifetime, the g-factor is more sensitive to the error in the lifetime. From the g-factor fit values of $\tau = 1.0 \pm 0.3$ ps and 0.7 ± 0.2 ps were found for the two targets. The average value of 0.8 ± 0.2 ps is in good agreement with the above value used in the analysis, which is a weighted mean quoted in ref. [20]) of two DSA measurements and one Coulomb excitation measurement.

(*iv*) *Hyperfine interaction coefficients* a_J. For the $^3S_1$ and the $^3P_1$ states these coefficients are not exactly known. The $a_J(^3S_1)$ coefficients used in the analysis (table 2) were taken from a relativistic Hartree-Fock calculation quoted in ref. [21]). Calculations of screening with the alkali approximation [15]) give values within 1 % of the Hartree-Fock value assuming that only the 2s electron is screened. The contribution to the error in the g-factor for ^{24}Mg (table 3) was obtained assuming an uncertainty in $a_J(^3S_1)$ of 3 %.

For the ^3P states the effects of screening are about 2 % and may be calculated with the alkali approximation. Different values of $a_J(^3P_1)$ are obtained for jj and LS coupling. Since it is not certain which coupling scheme applies for highly stripped ions, the average of the two values was used in the analysis of the data and the 8 % spread about this value was taken as the uncertainty. The contribution to the error in the g-factor for ^{24}Mg was small.

The contributions were taken to be the same for ^{20}Ne as for ^{24}Mg. This is a conservative assumption.

(*v*) *Coincident background*. For the ^{20}Ne measurements an extra error was introduced to allow for the uncertainty in the coincident background correction factor (see subsect. 3.1).

3.4.3. Populations of electronic states. Populations of the electronic states were deduced from the g-factor fits. The results for the different fits are displayed in table 4. The errors were calculated by taking into account the sources of error discussed in subsect. 3.4.2. The results of fits II and III for the populations of the $^3S_1$, $^3P_2$ and $^3P_1$ states in ^{24}Mg differ significantly from the relative statistical distributions taken for fit I. For another example of a deviation from the statistical distribution, see ref. [22]). The total population of the excited two-electron state, however, is the same for all three fits within the errors. From fig. 8 it is clear that it is difficult to determine the populations of the $^3P_2$ and $^3P_1$ states separately in fit III, because these states show such a similar structure.

Confirmation of the existence of a large population in the two-electron excited state of ^{20}Ne was given by the results of a time-integral measurement, in which the

TABLE 4

Measured populations of electronic states

Nucleus	Charge state	Fraction of total (%) [a]		Configuration	Term	Population α of state (%) Plunger measurement [b] fit I	fit II	fit III
$^{24}_{12}$Mg	12	2						
	11	10		$(1s)^1$	$^2S_{\frac{1}{2}}$	16 ± 2	13 ± 3	12 ± 3
				$(2s)^1$	$^2S_{\frac{1}{2}}$	2	2	2
	10	36		zero-field configurations				
				$(1s)^1(2s)^1$	$^3S_1$	33 ± 2 [c]	19 ± 4	21 ± 6
				$(1s)^1(2p)^1$	$^3P_2$		17 ± 3 [d]	9 ± 11
					$^3P_1$			8 ± 8
	9	38		$(1s)^2(2s)^1$	$^2S_{\frac{1}{2}}$	10	10	10
				$(1s)^1(2s)^1(2p)^1$	$^4P_{\frac{5}{2},\frac{3}{2},\frac{1}{2}}$			
				$(1s)^1(2p)^2$				
	8	12		$(1s)^2(2s)^2$	$^1S_0$			
		[e]	[f]			[g]	Spectrograph [h]	
$^{20}_{10}$Ne	10	4	6 ± 3					
	9	28	40 ± 5	$(1s)^1$	$^2S_{\frac{1}{2}}$	26 ± 8	36 ± 5	
				$(2s)^1$	$^2S_{\frac{1}{2}}$	4	4 ± 1	
	8	49	44 ± 4	zero-field configurations			16 ± 2	
				$(1s)^1(2s)^1$	$^3S_1$	31 ± 8	28 ± 3	
				$(1s)^1(2p)^1$	$^3P_{2,1}$			
	7	19	10 ± 3	$(1s)^2(2s)^1$	$^2S_{\frac{1}{2}}$	8	8 ± 3	
				$(1s)^1(2s)^1(2p)^1$	$^4P_{\frac{5}{2},\frac{3}{2},\frac{1}{2}}$		2 ± 1	
				$(1s)^1(2p)^2$				

[a]) Simplified Marion and Young [25]) type calculation [42]).
[b]) Fits I to III are explained in subsect. 3.4.1.
[c]) Statistically distributed: 9 %, 15 %, 9 %.
[d]) Statistically distributed: 11 %, 6 %.
[e]) Ref. [25]).
[f]) Average of two integral spectrograph measurements. The errors were estimated from the spread in values obtained for two measurements.
[g]) Weighted mean of the results with the two targets.
[h]) Integral spectrograph measurement described in subsect. 3.4.3.

γ-ray angular correlations were measured for each charge state separately. The ^{20}Ne ions produced in the reaction $^{12}C(^{12}C, \alpha)^{20}Ne$ with charges from 7+ to 10+ were separated in an Enge-type split-pole spectrograph at an angle of 9° to the beam direction and were detected simultaneously in four position-sensitive detectors (one for each charge state) in coincidence with α-particles detected at $\phi_\alpha = 135°$ to the beam direction. Gamma rays were detected in three 12.7 cm diam. by 12.7 cm long NaI(Tl) detectors in coincidence with α-particles and ^{20}Ne ions. Two NaI(Tl) detectors were rotated in the (x, y) reaction plane between angles $\phi = 55°$ and 120° and $\phi = 215°$ and 275° to the beam direction (x-axis). The third detector was set in two positions out of the reaction plane at angles $\theta = 0°$ and $\theta = 25°$, $\phi = 120°$.

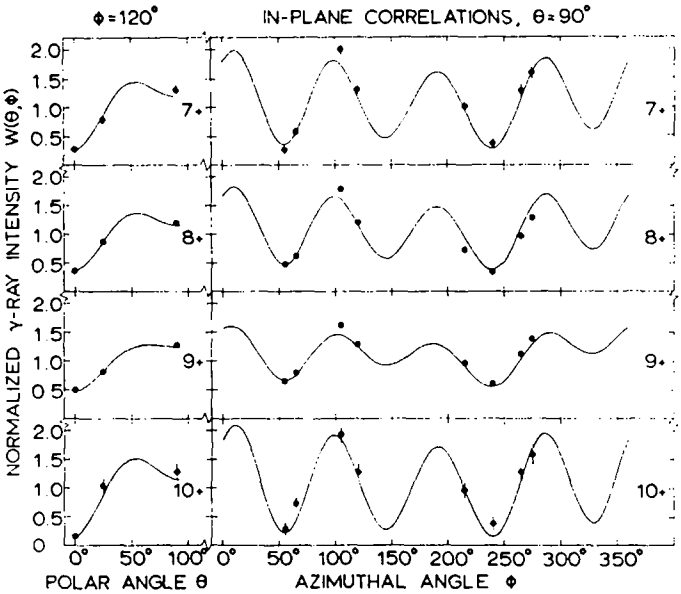

Fig. 13. Measured γ-ray angular correlations for the 7+ to 10+ ionic charge states of ^{20}Ne separated with a magnetic spectrograph. The z-axis is perpendicular to the horizontal (x, y) reaction plane defined by the beam direction and the ^{20}Ne detection angle (9° to the beam direction). The correlations were measured out of the reaction plane at an azimuthal angle of $\phi = 120°$ as well as in the reaction plane (polar angle $\theta = 90°$). The curves represent a simultaneous fit to the data as described in subsect. 3.4.3.

The γ-ray angular correlations measured for the four charge states are displayed in fig. 13. The data were fitted with eq. (6) with the inclusion of corrections for the finite opening angle of both the γ-ray detectors (Q_k coefficients) and the spectrograph and for the relativistic velocity of the ^{20}Ne nuclei. For each charge state only the population of the ground state and one excited state were taken into account. This is discussed below. The time-integral deorientation coefficients $G_k(\infty)$ for each electronic state were taken from eq. (5) for infinite time and for the value of the g-factor given in table 3. The density matrix elements in eq. (7) [four free parameters, i.e. two relative substate populations and two phase factors [18])], the relative populations of each ground and excited state (three parameters) and the normalization factor were determined from a simultaneous fit to all the measured correlations (40 data points). For single-electron ions only 1s and 2s configurations were included and for two-electron ions the populations of the $^3S_1$, $^3P_2$ and $^3P_1$ states were assumed to be statistical. For three-electron ions, in order to explain the rather large perturbation measured, it was found necessary to introduce an excited state with an unpaired 1s electron, in addition to the $(1s)^2(2s)^1$ ground state. Such a state might be given by the configurations $(1s)^1(2s)^1(2p)^1$, $(1s)^1(2p)^2$; (^{4}P), see for examples refs. [23, 24]).

The populations of the configurations obtained in this experiment and the charge state fractions extracted at the same time from the data are given in table 4. The agreement with the populations extracted from the time-differential data is excellent. The measured charge state fractions may also be compared with those calculated semi-empirically by Marion and Young [25]). There is a slight shift in the calculated charge distribution towards higher charge states. This could be due to the dependence of the charge distribution on the density and the atomic number of the target material [26]). For example, a plunger experiment carried out with ^{24}Mg ions recoiling through a thin layer of Ag showed a much lower population of the $(1s)^1$ state. Furthermore, a time-integral measurement in the slit geometry for ^{24}Mg on recoil through thin layers of various metals showed a marked dependence on the atomic number of the layer. Hence the experimental values for the charge state fractions in table 4 are to be preferred.

The spectrograph experiment showed that (63 ± 3) % of two-electron Ne ions at $v/c = 5.7$ % are in an excited state with a strong hyperfine interaction; (90 ± 3) % of the one-electron ions and (80 ± 6) % of the three-electron ions, however, are in their ground states. This surprisingly high fraction of two-electron excited ions was deduced with the value of the g-factor taken from the plunger experiment; the population from the plunger experiment itself with the total fraction (table 4) yielded an excited fraction of (70 ± 20) %. Similar fractions may be deduced for Mg ions from the data in table 4, although a spectrograph experiment has not been carried out.

A similar spectrograph experiment was performed by Goldring *et al.* [2]) for ^{18}O ions at about the same time as the ^{20}Ne experiment. The rotation of the angular correlation due to non-axial detection of the reaction products was compensated by shifting the symmetry axis deduced from the angular correlation with respect to the beam direction. The data were interpreted under the assumption of axial symmetry. This approximation alone, however, is not sufficient to account for the fact that the value (14–37 %) deduced for the population of excited two-electron states with a strong hyperfine interaction is appreciably lower than that deduced from the Ne experiment. The reason for this difference is not at present understood.

3.4.4. The lifetime measurements. The Ge(Li) detector at 0° to the beam direction served as a check on the lifetimes of the first-excited states. For ^{24}Mg the data were sufficiently good for a precision measurement. For ^{20}Ne, however, due to instability of the Ge(Li) detector caused by high counting rates and neutron damage, the data were not further analyzed. From the g-factor fits with the NaI(Tl) detectors values for the lifetimes were also extracted (see subsect. 3.4.2).

For ^{24}Mg the stopped fractions, i.e. the fractions of γ-rays detected from nuclei decaying in the stopper, are displayed as a function of target-stopper distance in fig. 14. Analysis of these data leads to a mean life of $\tau_m = 2.09\pm0.13$ ps. This value deviates from the compiled [27]) value (1.75 ± 0.08 ps), but agrees well with more recent measurements [28]). The various corrections included in the analysis are discussed below.

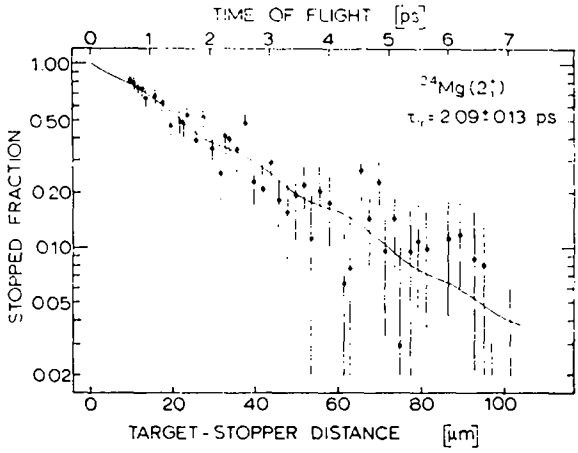

Fig. 14. Fractions of ^{24}Mg* nuclei decaying in the stopper as a function of perpendicular target-stopper distance measured with a Ge(Li) detector at 0° to the beam direction. The lifetime was determined by a least-squares fit to the data. The oscillation of the curve arises from the inclusion of deorientation effects calculated from the values of the g-factor and the populations of electronic states from the present work. The increasing errors towards larger target-stopper distances reflect the equal measuring time for each point necessary for an optimum determination of the g-factor.

Since the nuclear lifetime is comparable to the slowing-down time of the nuclei in the stopper, the tail of the stopped peak line-shape contributes to the intensity at the flight peak position. The correction on the intensity of the flight peak was estimated as follows. First the spectra were corrected for multiple Compton scattering of γ-rays emitted in flight. The line-shape of the stopped fraction was then extrapolated with a standard line-shape program [29]) to determine the contribution under the flight peak. This correction was always less than 6 %. The contents of the flight peak were further corrected for relativistic effects on both the opening angle and the efficiency of the Ge(Li) detector. Deorientation effects were also taken into account in the least-squares fit to the data, although these effects are small at 0° (less than 10%) in the present case. The values of the g-factor and of the populations of the electronic states were taken from the present work. The best χ^2 value for the fit was obtained for the same zero distance (with an error of 1.3 μm) as measured by eye. The weighted mean from four independent zero-distance measurements (see subsect. 3.4.2) was taken in the lifetime fit.

4. Theoretical discussion and conclusions

4.1. THEORETICAL DISCUSSION

Theoretical calculations of g-factors for the first-excited states of ^{24}Mg and ^{20}Ne are compared with the present experimental results in table 5.

For ^{24}Mg the single-shell ($1d_{\frac{5}{2}}$) and the modified surface delta interaction (MSDI) two-shell ($1d_{\frac{5}{2}}2s_{\frac{1}{2}}$) calculations [30]) differ by more than three standard deviations from

TABLE 5

Comparison of theoretical g-factors with experiment

	g-factor	
	$^{20}Ne(2_1^+)$	$^{24}Mg(2_1^+)$
Experiment	$+0.54 \pm 0.04$	$+0.51 \pm 0.02$
PHF [a])	$+0.54$	$+0.55$
PHF [b])		$+0.57$
SU(3) [c])		$+0.50$
Shell model calculations:		
Single shell ($1d_{\frac{5}{2}}$) [d])		$+0.58$
MSDI ($1d_{\frac{5}{2}}2s_{\frac{1}{2}}$) [d])		$+0.57$
Truncated: KLS [e]),		$+0.52$
MSDI/PW/Kuo/ASDI [f])		$+0.52$ to $+0.54$
Full space: MSDI [g]),	$+0.51$	
MSDI/PW/Kuo [f])	$+0.51$	$+0.51$ to $+0.53$

[a]) Ref. [31]). [b]) Ref. [32]). [c]) Ref. [35]). [d]) Ref. [30]). [e]) Ref. [34]). [f]) Ref. [33]).
[g]) Ref. [36]).

the experimental value. Projected Hartree-Fock (PHF) calculations [31,32]) also deviate significantly. The earlier experimental values for the g-factor [10,12]) ($g = +0.44 \pm 0.04$) led to the inclusion of the $1d_{\frac{5}{2}}$ configuration in the Utrecht calculations [33]). These calculations in a truncated space with MSDI, Preedom-Wildenthal (PW), Kuo and adjusted surface delta interaction (ASDI) matrix elements lead to values in good agreement with the present experiment. Another calculation in a truncated space with renormalized Kahana-Lee-Scott (KLS) matrix elements [34]) and an SU(3) calculation [35]) also agree with the present data.

Calculations in the full ($1d_{\frac{5}{2}}2s_{\frac{1}{2}}1d_{\frac{3}{2}}$) space all yield slightly lower values than the truncated calculations, in better agreement with the experimental value.

For ^{24}Mg it may thus be concluded that the $1d_{\frac{5}{2}}$ configuration contributes significantly to the g-factor of the first 2^+ state and that, as expected, calculations in the full sd space give somewhat better results. It is not yet possible to distinguish between various interactions for doubly even $T = 0$ nuclei because neither the theoretical nor the experimental values are precise enough.

For ^{20}Ne fewer calculations have been performed [33,36]) and the agreement with the experimental value is well within the experimental error.

4.2. CONCLUSIONS

The present paper shows that the time-differential recoil-into-vacuum technique can be used to measure g-factors of nuclei in excited states even for velocities at which only a 10–20 % fraction of single-electron ions is present. The data also show that about 70 % of the two-electron ions may be in an excited electronic state with a strong hyperfine interaction. This may enable the measurement of g-factors of higher-Z nuclei at velocities at which only low fractions of two-electron ions are present.

The g-factor would then be determined mainly from the high-frequency component arising from the two-electron excited states. It has further been demonstrated that integral measurements with charge-state separation yield useful information on charge-state distributions and excitation probabilities. This information can be used to facilitate and improve the interpretation of time-differential experiments. It should be noted that the assumption of a statistical distribution for the population of electronic states with about the same excitation energy may not necessarily be valid (see subsect 3.4.3).

It has been shown that the detection of particles in a slit-detector considerably improves the anisotropy of the γ-ray angular correlation for reactions with spinless particles for those cases in which the anisotropy for particle detection in an annular detector is spoiled by high angular momentum transfer from the incoming to the outgoing particle. In this geometry g-factors and also lifetimes of the order of 1 ps were determined, without separation of flight and stopped fractions, with high efficiency NaI(Tl) detectors at 90° to the beam.

The experimental value obtained for the g-factor of ^{20}Ne may also be used to calibrate the transient field in the high-recoil-velocity region where large deviations from the empirically adjusted Lindhard and Winter theory [9,37,38]) have been observed.

The authors wish to thank Dr. C. P. Bhalla for enlightening discussions on the atomic physics and J. E. Koops and J. F. A. van Hienen for fruitful theoretical discussions. The authors thank Prof. P. M. Endt for his continuing interest. They also thank N. van Zwol, D. Balke and J. Sodaar for the construction of the plunger and interferometer, J. P. Cooyman for the construction of the target chamber and J. A. Reynders for the preparation of the plunger foils. Further L. W. Wiggers, H. Aarts, P. G. Hogenbirk and W. Meijers are acknowledged for their assistance in parts of this work. The authors are grateful to E. du Marchie van Voorthuizen for valuable discussions on plunger techniques. One of us (H.A.D.) is grateful to the "Stichting voor Fundamenteel Onderzoek der Materie" (FOM) for a honorarium. This work was performed as a part of the research program of FOM with financial support from the "Nederlandse Organisatie voor Zuiver Wetenschappelijk Onderzoek" (ZWO).

References

1) M. A. Faessler, B. Povh and D. Schwalm, Ann. of Phys. **63** (1971) 577
2) G. Goldring *et al.*, Phys. Rev. Lett. **28** (1972) 763
3) W. L. Randolph *et al.*, Phys. Lett. **44B** (1973) 36
4) T. K. Alexander *et al.*, Phys. Rev. **C9** (1974) 1748
5) J. R. Beene *et al.*, Nucl. Phys. **A230** (1974) 141
6) J. Asher *et al.*, J. of Phys. **G1** (1975) 415
7) H. A. Doubt *et al.*, Proc. Int. Conf. on hyperfine interactions (Upplands Graviska, Uppsala, 1974) p. 93

8) Z. Berant *et al.*, Nucl. Phys., **A243** (1975) 519
9) J. L. Eberhardt, R. E. Horstman, H. A. Doubt and G. van Middelkoop, Nucl. Phys. **A244** (1975) 1;
J. L. Eberhardt, G. van Middelkoop, R. E. Horstman and H. A. Doubt, Phys. Lett.; **56B** (1975) 329
10) R. E. Horstman, J. L. Eberhardt, H. A. Doubt and G. van Middelkoop, Phys. Lett. **48B** (1974) 31
11) H. J. Andrä, Physica Scripta **9** (1974) 257
12) J. L. Eberhardt, R. E. Horstman, H. W. Heeman and G. van Middelkoop, Nucl. Phys. **A229** (1974) 162
13) N. Bohr, Phys. Rev. **58** (1940) 654; **59** (1941) 270
14) H. Frauenfelder and R. M. Steffen, in Alpha-, beta-, and gamma-ray spectroscopy, ed. K. Siegbahn, vol. 2 (North-Holland, Amsterdam, 1965)
15) H. Kopfermann, Kernmomente (Akademische Verlag, Frankfurt, 1956)
16) Z. Berant *et al.*, Nucl. Phys. **A178** (1971) 155
17) A. Bohr, Nucl. Phys. **10** (1959) 486
18) J. G. Cramer and W. W. Eidson, Nucl. Phys. **55** (1964) 593
19) F. Bosch and H. Spehl (Universität Freiburg), to be published
20) D. K. Olsen *et al.*, Nucl. Phys. **A220** (1974) 541
21) M. B. Goldberg, Physica Scripta **11** (1975) 184
22) C. P. Bhalla, D. L. Matthews and C. F. Moore, Phys. Lett. **46A** (1973) 336
23) D. J. Pegg *et al.*, Phys. Rev. **A9** (1974) 1112
24) C. F. Moore, W. J. Braithwaite and D. L. Matthews, Phys. Lett. **44A** (1973) 199
25) J. B. Marion and F. C. Young, Nuclear reaction analysis (North-Holland, Amsterdam, 1968)
26) H. H. Heckman, E. L. Hubbard and W. G. Simon, Phys. Rev. **129** (1963) 1240
27) P. M. Endt and C. van der Leun, Nucl. Phys. **A214** (1973) 1
28) C. Broude, F. A. Beck and P. Engelstein, Nucl. Phys. **A216** (1973) 603;
A. Johnston and T. E. Drake, J. of Phys. **A7** (1974) 898;
J. S. Forster *et al.*, Phys. Lett. **51B** (1974) 133;
D. Schwalm *et al.*, see E. K. Warburton, Proc. Int. Conf. on nuclear structure and spectroscopy, vol. 2 (Scholar's Press, Amsterdam, 1974) p. 506;
S. F. Biagi, W. R. Phillips and A. R. Barnett, Nucl. Phys., **A242** (1975) 160
29) J. A. J. Hermans *et al.*, Nucl. Phys., to be published
30) J. F. A. van Hienen and P. W. M. Glaudemans, Phys. Lett. **42B** (1972) 301
31) M. R. Gunye and C. S. Warke, Phys. Rev. **159** (1967) 885
32) M. R. Gunye, Phys. Lett. **37B** (1971) 125
33) G. A. Timmer, F. Meurders and J. E. Koops (Utrecht University), private communications
34) S. K. M. Wong, J. M. G. Gomez and A. P. Zuker, Phys. Lett. **42B** (1972) 157
35) D. Strottman, Phys. Lett. **39B** (1972) 457
36) E. C. Halbert, J. B. McGrory, B. H. Wildenthal and S. P. Pandya, Advances in nuclear physics, vol. 4, ed. M. Baranger and E. Vogt (Plenum Press, New York, 1971) p. 316
37) M. Forterre *et al.*, Phys. Lett. **55B** (1975) 59
38) M. Forterre *et al.*, Phys. Rev. **C11** (1975) 1976
39) R. Marrus, Nucl. Instr. **110** (1973) 333
40) W. L. Wiese, M. W. Smith and B. M. Glennon, Report NSRDS-NBS **4** (1966) vol. 1;
W. L. Wiese, M. W. Smith and B. M. Miles, Report NSRDS-NBS **22** (1969) vol. 2
41) I. A. Sellin, M. Brown, W. W. Smith and B. Donnally, Phys. Rev. **A2** (1970) 1184
42) H. D. Betz, Rev. Mod. Phys. **44** (1972) 465;
A. B. Wittkower and H. D. Betz, Atomic Data **5** (1973) 113;
I. S. Dmitriev and V. S. Nikolaev, JETP (Sov. Phys.) **20** (1965) 409
43) Landolt-Börnstein, Zahlenwerte und Funktionen, Band I, Teil 1 (Springer, Berlin, 1950) p. 48